

Four-decade response of land surface temperature to urban expansion in Beijing



Yibing Wang^{a,b}, Xianhong Xie^{a,b,*}, Xiang Zhao^{a,b}, Shunlin Liang^c, Bowen Zhu^d, Arken Tursun^{a,b}, Fuxiao Jiang^{a,b}, Yao Liu^{a,b}, Xiaotong Zhang^{a,b}

^a State Key Laboratory of Remote Sensing Science, Beijing Normal University, Beijing 100875, China

^b Beijing Engineering Research Center for Global Land Remote Sensing Products, Institute of Remote Sensing Science and Engineering, Faculty of Geographical Science, Beijing Normal University, Beijing 100875, China

^c Department of Geography, University of Hong Kong, Hong Kong

^d College of Water Science and Engineering, Taiyuan University of Technology, Taiyuan 030024, China

ARTICLE INFO

Keywords:

Land surface temperature
Satellite product
Integration of physical modeling
Urban expansion
Heat stress and phenology
Beijing

ABSTRACT

Urban expansion with increased impervious surface area (ISA) can affect the thermal regimes by altering the water and energy balance. Previous studies have indicated that ISA is the primary surrogate of rising land surface temperature (LST). However, urban-induced LST changes are not yet well quantified because of the temporal limitations of the LST datasets and the uncertainties from climate variabilities. In this study, we integrated multiple satellite-based products (vegetation coverage, albedo and radiation forcing) into a physically-based land surface model i.e., Variable Infiltration Capacity (VIC), to detect multi-temporal scale response of LST to the increasing ISA in Beijing. Heat transfer-related parameters in the model were updated along with urbanization processes. The integrated modeling presented high performance for simulating LST, as evaluated with ground-based observations and the MODerate-resolution Imaging Spectroradiometer (MODIS) LST product. We found that the average LST over Beijing increased from 10.3 °C in 1980–1990 to 11.2 °C in 2010–2020, with nearly 33% contributed by the urban growth. The urban-induced thermal effect was particularly strong in summer daytime and winter nighttime. The frequency of heat days (the day with the maximum LST over 40 °C) in a year for Beijing appeared to linearly correlate with the impervious surface fraction (ISF) when ISF > 25%. For the urbanizing area, moreover, the four-decade LST estimates indicated that the annual overheating duration was obviously extended with a rate of about 5 days per decade. We therefore conclude that the urban expansion in Beijing not only amplified heat stress but also altered heat phenology, which have implications for urban planning and the construction of heat mitigation facilities.

1. Introduction

Urban expansion is characterized by the fact that over 55% of the population currently live in cities, comparing to 5% in 1900 (UN, 2018). Urban space has relatively more impervious surface area (ISA) and lower vegetation coverage than the natural and agricultural land (Santamouris, 2020), thereby regulating albedo, reducing evaporation cooling effect and land cover heat capacity, and exacerbating heat production (Hao et al., 2018; Miles and Esau, 2020; Peng et al., 2018). Additionally, high-dense buildings can increase the aerodynamic roughness, decreasing the wind speed and heat removing (Hao et al., 2018). The combination of high heat production, air retention, and additional heat

introduced by human activities can be directly reflected in land surface temperature (LST), consequently increasing overheating risks in urban regions (Manoli et al., 2019; Zhou et al., 2018).

The intensified LST in urban region has gained intensive attention. The surface urban heat island (SUHI), which represents the impact of urban growth on LST, has been documented in thousands of cities around the world since 1972 (Jiang et al., 2020; Li et al., 2022; Phelan et al., 2015; Rao, 1972; Santamouris, 2020; Zhou et al., 2022). These cases demonstrated intensive LST changes with the increasing ISA, as well as the SUHI diversity among various landscape composition and temporal scales, i.e., daytime/nighttime and seasonal differences (Manoli et al., 2019; Miles and Esau, 2020; Niu et al., 2020). For

* Corresponding author.

E-mail address: xianhong@bnu.edu.cn (X. Xie).

instance, Cao et al. (2017) and Morabito et al. (2021) found that humid cities show stronger SUHI effects during the daytime, while coastal cities may have less SUHI due to the mitigating effect of the sea. And the SUHI generally presents variable patterns among daytime/nighttime and seasons (Cui et al., 2017; Yang et al., 2013; Zhou et al., 2010), and shows more variability during the daytime (Niu et al., 2020; Zhao et al., 2014).

However, previous studies of quantifying SUHI were generally based on the LST difference between urban/suburb regions or local climate zones (Oke and Stewart, 2012; Zhou et al., 2018). This is the so-called space-for-time approach used to detect urban heat island, assuming that climate induced LST difference between adjacent regions is negligible, as adjacent regions often have similar climate conditions (e.g., wind speed, shortwave radiation, and air pressure) (Yuan et al., 2022). This assumption may be valid for small scales, but holds uncertainties from the climate variability and the boundary definition for a large area (Kim and Brown, 2021; Meng et al., 2018). Moreover, ground-based observations and satellite retrievals, which are the mainstream datasets for LST and SUHI detection, may also bring substantial uncertainties (Niu et al., 2020; Zhou et al., 2018). Ground-based observations are often limited to a specific location and fail to capture temperature variations over a broader domain. Satellite retrievals may be subject to a variety of uncertainties from sensor quality, weather condition, revisit time gaps, spatial discontinuities, and short time span (Li et al., 2023; Meng et al., 2018; Niu et al., 2020).

Alternatively, physical-based models have been proposed for LST estimation with relatively high temporal resolutions (Ji et al., 2021; Li et al., 2019; Masson et al., 2020). They have the advantage to provide seamless LST estimates, and to isolate LST response to urbanization with hypothetical scenarios. Multiple researches have demonstrated favorable performance of physical models in identifying LST changes to the land cover transformation (Meili et al., 2021; Mishra et al., 2010). Currently, however, previous model-based studies usually used constant physical parameters (e.g., albedo, leaf area index [LAI]), and only considered two scenarios regarding pre-urbanization and post-urbanization conditions. Urban growth is a continuous process, the modeling should reflect urban and other land cover dynamics along with associated parameters change for conducting a reasonable LST simulation and overheating risk analysis (Pumo et al., 2017).

In this study, we employed a physical land surface model, i.e., Variable Infiltration Capacity (VIC) model for LST estimation. The VIC model has been successfully used to identify LST in urban areas in the White River Basin, Indiana (Yang et al., 2010; Yang et al., 2011) and upper Midwest United States (Mishra et al., 2010). Moreover, we updated the land cover types every five years, and four thermal-related parameters (LAI, fractional vegetation cover [FVC], albedo, and downward shortwave radiation [DSR]) every day to reflect the continuous process of urbanization in the modeling process. We chose Beijing as a study area as it is a typical city with rapid urbanization in China, and its LST patterns and urban-induced LST changes are noteworthy (Peng et al., 2016; Quan et al., 2014; Yang et al., 2013). Previous studies achieved inconsistent statement among diurnal (Meng et al., 2018; Wang et al., 2017) and seasonal SUHI comparisons (Hu et al., 2015; Liu et al., 2020b; Wang et al., 2017; Yang et al., 2014) in Beijing due to limitations in space-for-time approach and temporal resolution. Based on the integrated modeling, our work estimated four decades of LST with 3-hour resolution, and identified the response of LST to urbanization at multi-temporal scale (annual, seasonal and diurnal) and the overheating phenology change in Beijing. Please note many factors may exert impact on LST (e.g., urban configuration, urban-climate feedbacks), yet our study focused on the impact of changes in land cover conditions (i.e., land cover types and associated thermal parameters) on LST. The findings from this study are expected to give implications for urban planning and heat mitigation strategies in Beijing and other cities with similar urbanization progresses.

2. Study area and data

2.1. Study area

Beijing is located in the northeastern China between 39.43–41.05°N and 115.42–117.50°E, with the total area of about 16,600 km² (Fig. 1). It has a warm monsoon climate and four distinct seasons, which is characterized with cold and windy winter, and hot and humid summer. The annual mean temperature is about 11 °C, and precipitation is approximately 500 mm during the past four decades. According to the Eleventh Five-Year Plan, Beijing can be divided into four functional zones: The Core Functional Zone (Core-Zone, ~94 km²), the Urban Functional Extended Zone (Extended-Zone, ~1289 km²), the New Urban Development Zone (NewDev-Zone, ~6322 km²), and the Ecological Conservation Zone (Eco-Zone, ~8880 km²). The Core-Zone is a symbol of politics and culture, with a lot of historic buildings, the Extended-Zone and NewDev-Zone function as the commerce and education, and the Eco-Zone serves as a green ecological barrier with little human intervention.

Beijing has experienced rapid urbanization. Its permanent population was approximately 9 million in 1980 and up to 21 million in 2019, and its urban space increased from approximately 1448 km² to 3686 km² during 1980–2015 (Wang et al., 2020). Under such population explosion and urbanization, urban environment related disasters (e.g., overheating, flooding) became more frequent and intensive nowadays. A typical example was the overheating event in May 29, 2014, with the maximum air temperature up to 41.1 °C, causing the stressful emergency department visits and electricity demand. The overheating events (e.g., heat days, heat waves) may cause serious impact on the quality and comfort of urban living (Qiao et al., 2014).

2.2. Data

2.2.1. Data for model input

The data for model input includes topographical data, meteorological forcing, soil and land cover (i.e., vegetation) distribution maps and parameters. Table 1 lists the sources of the data for model input and for model evaluation. The topographical data (i.e., the digital elevation model) was obtained from U.S. Geological Survey (USGS) with the 90 m resolution (Danielson and Gesch, 2011), which was used to interpolate meteorological data. The meteorological data include precipitation, maximum and minimum air temperature, wind speed, and humidity, and they were from Zhu et al. (2021) with a spatial resolution of 0.0625°. The data were produced by interpolating observation stations from China Meteorological Administration (CMA) and have been evaluated over China with encouraging reliability (Meng et al., 2020; Xie et al., 2015). The measurements for precipitation, air temperature, wind speed and humidity were taken at different heights of 2 m, 1.5 m, 10–12 m and 1.5 m, respectively.

The soil map was generated based on a 30 arc-second-resolution soil characteristics dataset (Dai et al., 2013; Wei et al., 2013). The soil physical parameters such as field capacity, saturated hydraulic conductivity, and bulk density were derived based on a China soil dataset (Wei et al., 2013; Zhu et al., 2020). The other soil parameters (e.g., bubbling pressure, thermal damping depth) were defined according to the soil dataset from Food and Agriculture Organization (FAO) (Nijssen et al., 2001).

The land cover data in this study included base maps, urban (i.e., ISA) maps, and relevant parameters. The base maps were obtained from Liu et al. (2010), which were created by merging Landsat TM digital images with spatial resolution of 1 km and land cover of 12 types. These base maps may render substantial bias due to the coarse resolution (Gong et al., 2019), in particular, the dynamic of ISA is an important factor in this study, requiring high-precision distribution information. Therefore, the base maps were overlaid with the ISA maps with spatial resolution of 30 m from Wang et al. (2020) to achieve land cover maps

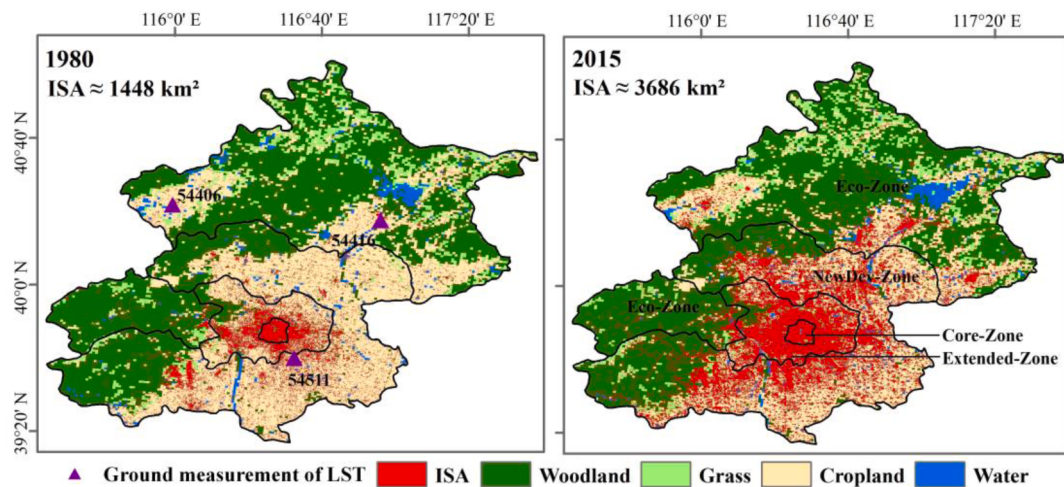


Fig. 1. The land cover maps of 1980 (left) and 2015 (right), three ground meteorological stations for LST measurement, and four function zones of Beijing. The abbreviations ISA donate impervious surface area.

Table 1
Overview of model input and verification data.

Data	Data source	Data usage
Digital Elevation Model (DEM)	U.S. Geological Survey (USGS)	Data interpolation
Meteorological forcing data	China meteorological administration (CMA)	Model forcing
Vegetation data	Urban map: Wang et al. (2020) Base map: Liu et al. (2010) Parameters*: Zhu et al. (2021)	Model forcing
Soil data	Soil cover map: Zhu et al. (2021) Soil parameters: China soil dataset and Food and Agriculture Organization	Model forcing
Downward shortwave radiation (DSR)	Global Land Surface Satellite (GLASS)	Additional forcing
Albedo	GLASS	Additional forcing
Leaf area index (LAI)	GLASS	Additional forcing
Fractional vegetation cover (FVC)	GLASS	Additional forcing
MODIS Terra LST	https://modis.gsfc.nasa.gov/	Model evaluation
LST gauge observations	CMA	Model evaluation

* The parameters of k and C_s for ISA were calibrated based on the MODIS LST product.

for model input. These ISA maps were created by Classification Regression Tree (CART) method using Landsat images.

In addition, four satellite products, that are DSR, albedo, LAI, and FVC, were integrated into the physical model. They were obtained from Global Land Surface Satellite (GLASS) products (<http://www.geodata.cn/thematicView/GLASS.html>) (Liang et al., 2021). GLASS DSR is generated based on a direct-estimation method from Wang et al. (2015), and it derived by the MODerate-resolution Imaging Spectroradiometer (MODIS) top-of-atmosphere (TOA) spectral radiance data and viewing geometry (Zhang et al., 2019). The GLASS albedo is also generated by the direct-estimation method, which established a relationship between the broadband albedo and TOA reflectance. The GLASS LAI is created using General Regression Neural Networks (GRNNs) with an entire-year preprocessed reflectance data, which are trained using integrated LAI series and MODIS or Advanced Very High Resolution Radiometer (AVHRR) reflectance data (Xiao et al., 2016). GLASS FVC is based on a multivariate adaptive regression splines

(MARS) method that used training samples generated from global sampled Landsat data (Jia et al., 2019). The four products have been used in multiple researches, e.g., integrating with physical models (Wang et al., 2020; Wu et al., 2020; Zhu et al., 2021), investigating land surface-atmosphere interactions (Guli et al., 2015; Zhang and Liang, 2018), and detecting environmental changes (Piao et al., 2015; Zhu et al., 2016). The datasets used in this study were at 0.05° spatial resolution. The DSR dataset is at daily temporal resolution, and the other three are at 8-day temporal resolution (Liang et al., 2021; Liu et al., 2013; Xiao et al., 2016; Zhang et al., 2016; Zhao et al., 2013).

2.2.2. Data for model evaluation

The physical model was validated using LST observations from three ground meteorological stations and a satellite LST product. The observed LST was obtained with a platinum resistance sensor that was partly buried in soil. The sensor can measure temperature at skin surface four times each day (02:00, 08:00, 14:00, 20:00), and output the average value of these four as ground surface temperature. This study used three ground stations with a long-time coverage (1980–2018): Beijing (ID 54,511, 39.81°N, 116.47°E), Yanqing (ID 54,406, 40.45°N, 115.97°E), and Miyun (ID 54,416, 40.38°N, 116.87°E). The Beijing station was built on impermeable surface, and the other two stations were located on grass-covered land type.

The satellite LST product was from the MODIS Terra, MOD11A2 v006, (<https://modis.gsfc.nasa.gov/>). This product adopted a generalized split-window algorithm by optimizing the observation angle and range of water vapor column contents (Wan et al., 2002). It has been demonstrated with acceptable performance in SUHI estimation and related biological and ecological researches, and is the one of the most commonly used data for LST and SUHI studies (Bounoua et al., 2015; Liu et al., 2020a; Morabito et al., 2021; Zhou, 2018; Zhou et al., 2010). MOD11A2 provides two instantaneous LST estimates (10:30 and 22:30 local solar time) every eight days at 1 km resolution. The data were initially released in 2000, but had much missing data in the first two years (Hu et al., 2015).

3. Methods

3.1. Physical model description

A few Land surface models (LSMs) have been applied for LST estimation in cities, e.g., Community Land Model Urban (Oleson and Fedde, 2020), Weather Research and Forecasting and Town Energy Balance (TEB) Model (Giannaros et al., 2018; Meyer, 2020), Surface

Urban Energy and Water balance Scheme (Li et al., 2016a; Sun and Grimmond, 2019). As one of the LSM models, the VIC model can effectively estimate water and energy balance along with the heat transfer from land surface to deep soil profile (Liang et al., 1994). The model has been widely used for water and energy balance estimation (Jiang et al., 2022; Wang et al., 2022; Zhu et al., 2023). It divides a study area into Latitude-Longitude grid cells, which are regarded as independent units for simulations (Liang and Xie, 2001). Each independent unit considers one main soil type, and multiple soil depths and vegetation types (Liang et al., 1994; Liang et al., 1996). The VIC can further capture realistic land cover and radiation dynamics coupling with remote sensing data, and the detailed information will be described in Section 3.2.

For each land cover type and soil layer, the initial surface temperature was set to be equal to air temperature to calculate the energy fluxes (e.g., evaporation, net radiation). These obtained fluxes were then used to calculate land surface temperature based on the Eqs. (1)–(3). Then, the estimated land surface temperature was used to recalculate the energy balance terms (e.g., evaporation, net radiation). The calculation will repeat until energy balance is achieved:

$$R_n = H + \rho_w L_e E + G = (1 - \alpha) R_s + \epsilon (R_L - \sigma LST^4) \quad (1)$$

where R_n is the net radiation, H is the sensible heat flux, ρ_w is the density of water, L_e is the latent heat of evaporation of water, E is the evaporation, G is the surface heat flux, α is the surface albedo, R_s is the downward shortwave flux, ϵ is the emissivity, R_L is the downward longwave flux, σ is the Stefan-Boltzmann constant. H and G is formulated as,

$$H = \frac{\rho_a c_p}{r_h} (LST - T_a) \quad (2)$$

$$G = \frac{\frac{k}{D_2} (LST - T_2) + \frac{C_s D_2}{2\Delta T} (LST - T_1^-)}{1 + \frac{D_1}{D_2} + \frac{C_s D_1 D_2}{2\Delta k}} \quad (3)$$

Where ρ_a is the atmospheric density, c_p is the atmospheric specific heat under normal pressures, r_h is the aerodynamic impedance, T_a is the air temperature, k is the thermal conductivity, C_s is the volumetric heat capacity, D_1 and D_2 is the thicknesses of two soil layers, T_1^- is the soil temperature at the end of the period at depth D_1 , and T_2 is the soil temperature at depth D_2 . The equations for other fluxes are not shown in this article, readers can refer to Liang et al. (1994) for more details.

Referring to Wang et al. (2020) and Taha (1999), the rainfall-runoff conversion process and thermal-related parameters (albedo, k , and C_s) are impactful to water and energy balance, and associated heat transfer including LST and heat fluxes. The official version of VIC model is able to estimate urban LST after adjusting the heat transfer process and related parameters according to characteristics of cities. Specifically, the surfaces albedo was derived from the GLASS product (mentioned in Section 2.2.1). The parameters of k and C_s for ISA vary with different urban structure (Mishra et al., 2010; Yang et al., 2010). The two were referring to Yang et al. (2010), and further calibrated based on the MODIS LST product for every land cover map, the values were between 2.5~4.5 W m⁻¹ K⁻¹ for k , 1.1~3.5 MJ m⁻³ K⁻¹ for C_s . The modified VIC model has been successfully implemented for LST calculation in cities (Mishra et al., 2010; Yang et al., 2010).

3.2. Integration with satellite products

The VIC model was run at the spatial resolution of 0.0625° (~5 km) and the temporal resolution of 3 h for the period of 1980–2020. To reflect land cover dynamics in Beijing, the land cover maps (i.e., the base maps merged with the ISA maps, as described in Sections 2.2.1) and associated parameters (e.g., k , C_s , root depth and fraction, and fraction of land use type) were updated every five years during the study period. Specifically, the maps and parameters were used to depict the land cover

conditions from that year to the next four (e.g., the map and parameters for the year of 1980 represented the land cover conditions for the years of 1980–1984).

As shown in Fig. 2, the four satellite-based additional parameters or forcing data (i.e., DSR, albedo, LAI, and FVC) were integrated with the model at daily time step. These products with the 8-day temporal resolution were linearly interpolated to daily values. Eight sets of land cover maps and parameters, as well as four daily additional parameters were used for characterizing realistic urban process in Beijing through the period of 1980–2020.

3.3. Detection of the urbanization effect on LST

To explore the LST dynamics and the urban growth effect on LST changes in Beijing, our study performed a comparative experiment with two scenarios (Fig. 2). The scenario that integrated multiple satellite products with the model is referred to as the “Urbanization” scenario, as described in Section 3.2. This scenario aimed to depict the real urban growth in Beijing during the study period.

For the comparative experiment, the other scenario was denoted as the “No-Urbanization”, which assumed no urban expansion in Beijing. This scenario thereby used a constant land cover map and parameters of 1980 for the whole study period, without considering the changes in LAI, FVC, and albedo. The DSR is not influenced by land surface conditions, so it was updated same as the “Urbanization” scenario. Under the first-order approximation, the LST Difference (LSTD) between the “Urbanization” and “No-Urbanization” scenarios can be assumed to represent the response of LST to urban growth. It is worth noting that the LSTD and SUHI are indexes both quantifying the impact of urbanization on LST, but the former adopts the LST difference between “No-urbanization” and “Urbanization” scenarios, while the latter refers to the regional LST difference based on a space-for time approach. Moreover, our work focused on the effect of urbanization on LST during 1980–2020 period, while climate change (characterized with global warming) should also play an important role during the period. We will further discuss it in Section 5.2.

To characterize the overheating consequences of the urban growth, the frequency of heat days (FHD) was proposed in our study. A heat day is defined as the day when the maximum LST exceeds 40 °C (Ding et al., 2010). The FHD is defined as the percentage of heat days in a year (365 or 366 days in a leap year). The relationship between the FHD and the regional urbanization ratio (i.e., ISF) was detected under the “Urbanization” scenario for the 2015–2020 period. The ISF was calculated by aggregating the Landsat-based ISA results (30 m) as fractional cover information in 0.0625° grid cells. The overheating durations and annual peak-LST day were further adopted in our work for understanding the phenology of overheating phenomenon in Beijing. The overheating duration is referred to as the days between the start and end of heat waves (Ding et al., 2010). Specifically, the beginning of the overheating duration is defined as the fifth heat day, and the last day of the duration is the fifth-to-last heat day of the year. Please note that the overheating duration indicates a period with generally high LST, rather than that all days during the period are heat days. The timing of peak-LST day is defined as the day with the highest LST in a year.

4. Results

4.1. Model evaluation

The simulated LST was first calibrated with the MODIS LST, and evaluated with the ground observations. The comparison with the MODIS LST was conducted for the period of 2002–2020 due to the missing data of MODIS in 2000–2001. To make a reasonable comparison, the MODIS LST data at 10:30 and 22:30 local solar time were compared with simulated average LST at 9:00–12:00 and 21:00–24:00, respectively, and they were assumed as morning time and evening time

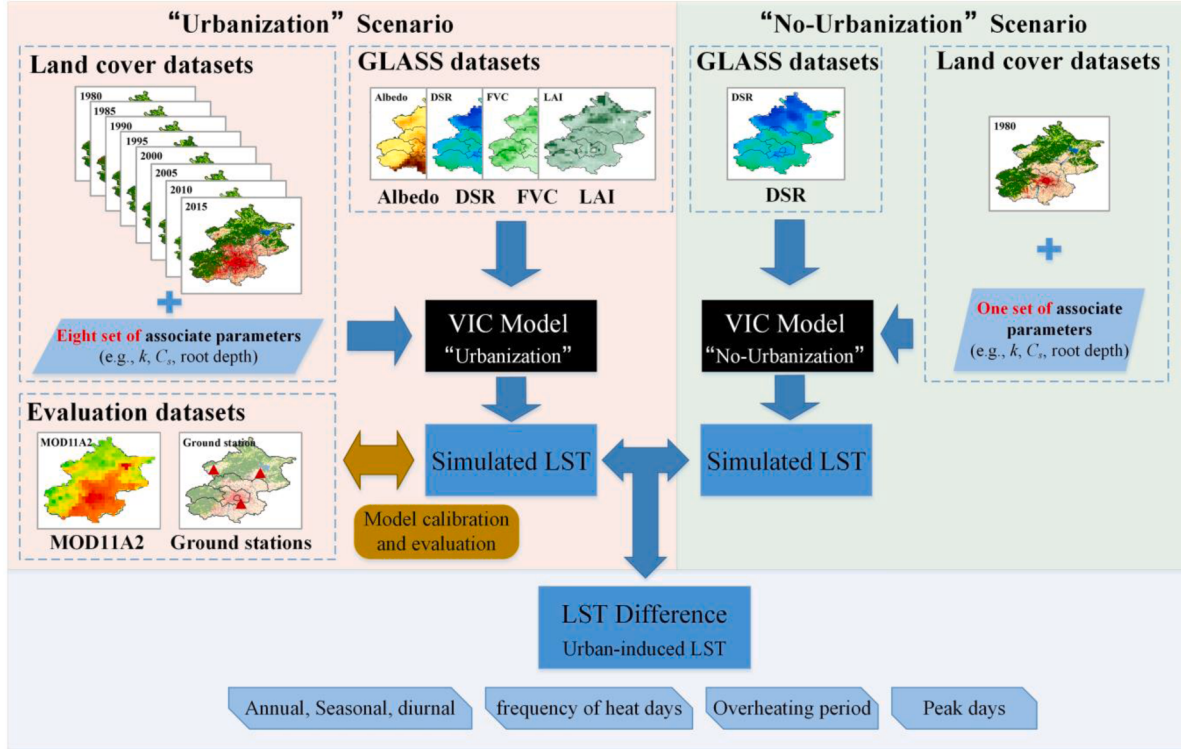


Fig. 2. Workflow of integrating the VIC model with multiple satellite products, and the comparative experiment setting. Topographical, meteorological forcing, and soil parameters are not shown in the figure, as they are same in the scenarios and can be found in Section 2.2.1.

comparison. And the MODIS LST data is upscaled to the same resolution of the simulated LST at 0.0625° . Three measures of Root Mean Squared Error (RMSE), relative bias (Bias), and correlation coefficient (R) were used to evaluate the performance of the VIC simulation.

As shown in Fig. 3, the simulated LST exhibits similar spatio-temporal patterns with the MODIS estimates for both the morning time and the evening time. For the morning time, the RMSE is 3.49°C , Bias is -12.1% , and the R is 0.98 for the time series comparison. Both the VIC model and MODIS present high LST in the city center (i.e., the Core-

Zone), with a decreasing gradient in the southwest-northeast direction, and their spatial consistency, which is represented with the correlation coefficient R , is approximately 0.90. As for the evening time, the VIC simulation fails to capture the scattered LST patterns in Eco-Zone, but grasps similar LST distribution in the other three zones with a spatial consistency about 0.72. As for the time series comparison, the RMSE, Bias and R is approximately 2.0°C , 26.2% , and 0.97, respectively.

For the station scale evaluation, the simulated LST presents similar temporal dynamics with the observed time series (Fig. 4). Please note

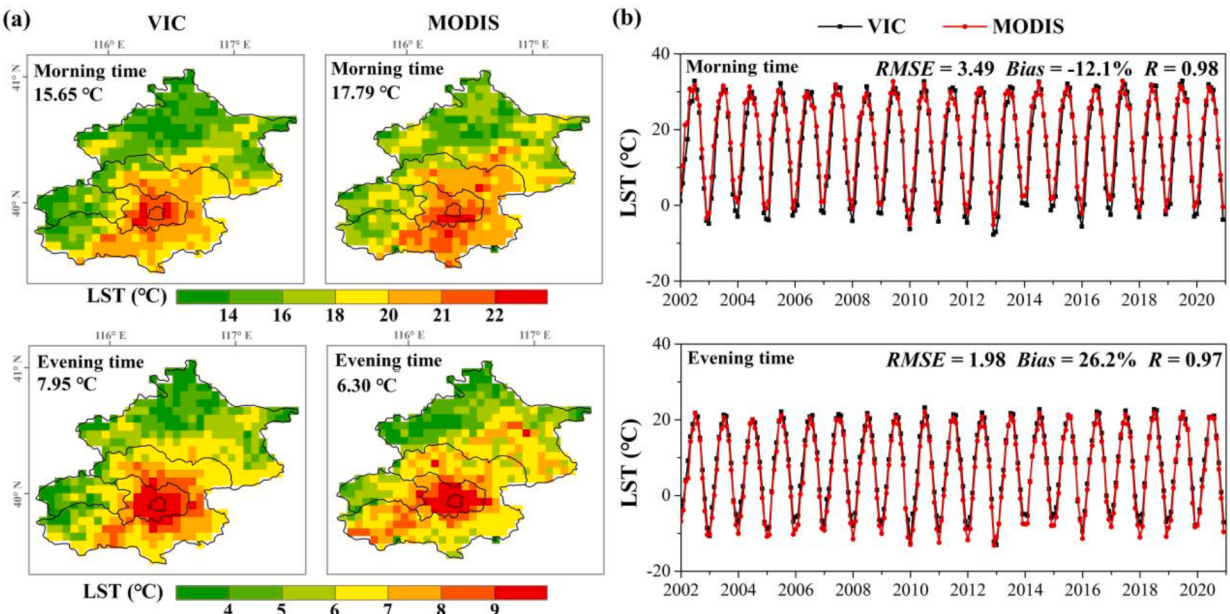


Fig. 3. Comparison of the simulated LST with the multi-year mean MOD11A2 product at morning time and evening time.

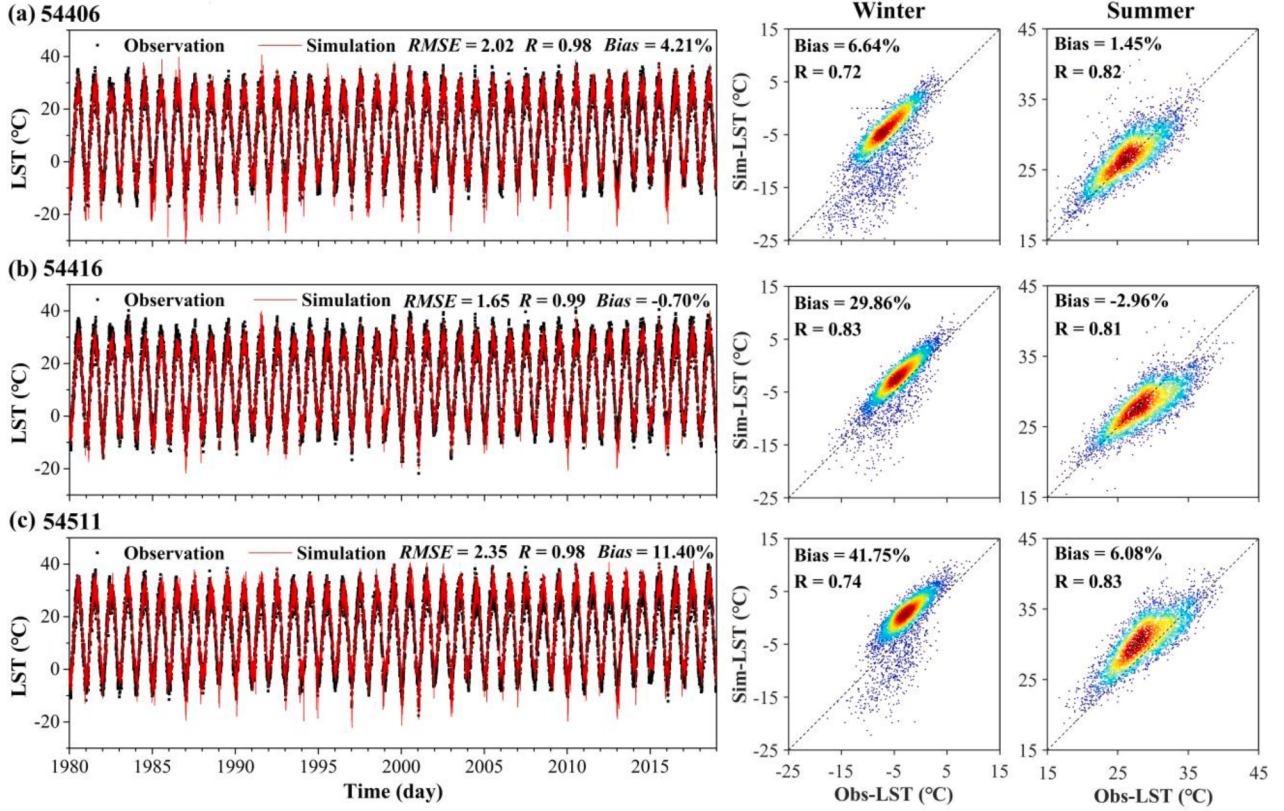


Fig. 4. The simulated LST validated by the ground-based observations.

the LST measurement was at point scale, which is smaller than the model output resolution. In order to relieve the mismatch of spatial scale, the evaluation was conducted at sub-grid scale with the same vegetation

type in the corresponding grid cell, since the physical processes regarding water and energy balances in VIC are formulated at sub-grid scale.

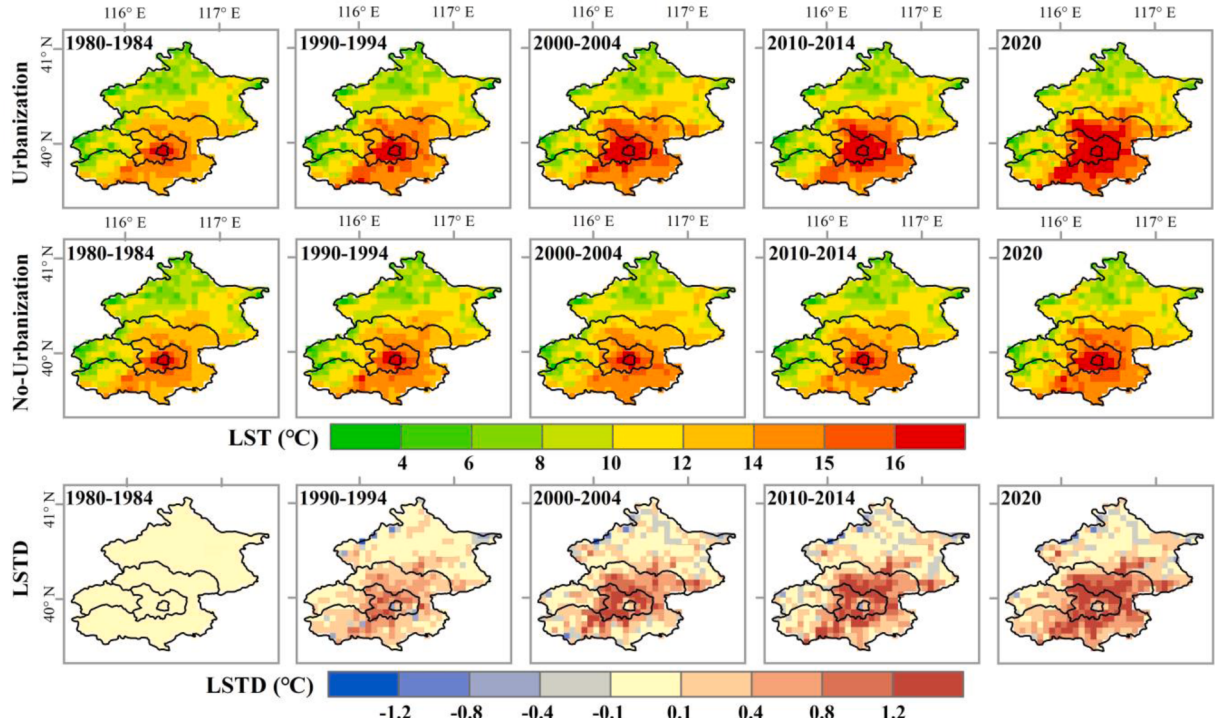


Fig. 5. The spatial distribution of LST for the “urbanization” (top) and the “no-urbanization” (middle) scenario, and the LSTD (bottom) in Beijing. The periods from left to right are 1980–1984, 1990–1994, 2000–2004, 2010–2014, and 2020.

The three evaluation indexes exhibit satisfactory values of *RMSEs* lower than 2.5 °C, *Rs* higher than 0.98, and *Bias* lower than 12%. However, the simulated LST shows an obvious overestimation at station 54,511 in winter season (> 40%): the average LSTs are about -1.6 °C and -2.8 °C for the simulations and the observations, respectively. Moreover, the simulated LST presents an encouraging feature with *Rs* higher than 0.70, and *Bias* values lower than 30% in summer for the other two stations. Overall, after integrating the remote sensing datasets, the VIC model demonstrated a satisfactory performance for the LST simulation, and the model and associated parameters were therefore used to identify the thermal effect of the urban growth in Beijing.

4.2. Interannual response of LST

After the model evaluation, long-term and 3-hourly LST estimates were obtained from the “Urbanization” and “No-Urbanization” simulation scenarios (Fig. 5). Both the scenarios show increase trends of LS. For the “Urbanization” scenario, the region with high annual LST (>16 °C) spreads from the Core-Zone to the surrounding regions. Especially for the year after 2010, approximately the whole Extended-Zone and half NewDev-Zone show high LST. However, the LST shows less changes in the “No-Urbanization” scenario during the 1980–2020 period, and the high LST only occurs in the Core-Zone.

As shown in Fig. 6, the long-term average LST was about 10.9 °C in Beijing during 1980–2020, and it was high in the Core-zone (17.2 °C) and low in the Eco-Zone (9.4 °C). Moreover, the average LST increased from approximately 10.3 °C during 1980–1990 to 11.2 °C during 2010–2020 in Beijing. The largest increase of LST appeared in the Extended-Zone (1.9 °C/yr) and the NewDev-Zone (1.2 °C/yr). For the “No-Urbanization” scenario (i.e., under the effect of climate change), the annual LST was approximately 10.7 °C in Beijing during 1980–2020. The LST of the whole Beijing increased approximately 0.6 °C from the period 1980–1990 to the 2010–2020, and it also largely increased in the

Extended-Zone (~0.9 °C) and the NewDev-Zone (~0.7 °C).

When comparing the LST between the “Urbanization” and “No-Urbanization” scenarios during 1980–2020 period (Fig. 6), the average LST Difference (LSTD) between the two scenarios was approximately 0.2 °C in Beijing, with the largest value in the Extended-Zone (~0.9 °C). The Eco-Zone showed the smallest average LSTD of approximately 0.04 °C. Moreover, the LSTDs presented increasing trends in Beijing and the four zones. The whole area of Beijing showed an increase trend of LSTD (~0.008 °C/yr), and the Extended-Zone and the NewDev-Zone exhibited the highest increase trends among the four zones, which were approximately 0.033 °C/yr and 0.016 °C/yr, respectively. The trends in the Core-Zone and Eco-Zone were less than 0.002 °C/yr.

4.3. Seasonal and diurnal response

We further detected the spatial distribution of the seasonal LSTDs in daytime and nighttime for 2015–2020 (Fig. 7). The LSTD showed spatial variability, with higher values in the Extended-Zone and NewDev-Zone. The nighttime LSTD was generally higher than the daytime value, except for the summer season. Specifically, the nighttime LSTD ranged between 0.4–0.9 °C, with the highest value in winter (~0.9 °C). The daytime LSTD exhibited significant seasonal changes (ranged between 0.0–0.8 °C), and showed the highest value in summer season (~0.8 °C), and low values in winter and spring seasons (<0.1 °C).

The Extended-Zone and the NewDev-Zone have the largest urban expansion in terms of the ISA increase. According to the results in Section 4.2 and Fig. 7, moreover, the two zones exhibited the highest LSTD among the four zones in Beijing. Therefore, we further detected the seasonal and diurnal characteristics of LSTD in the two zones during 2015–2020 period. As shown in Fig. 8, the highest LSTD occurred in summer daytime (~4.5 °C for the Extended-Zone and ~2.5 °C for the NewDev-Zone). For the seasonal comparison, the summer season (June to August) showed the highest LSTD values, with the average LSTD of

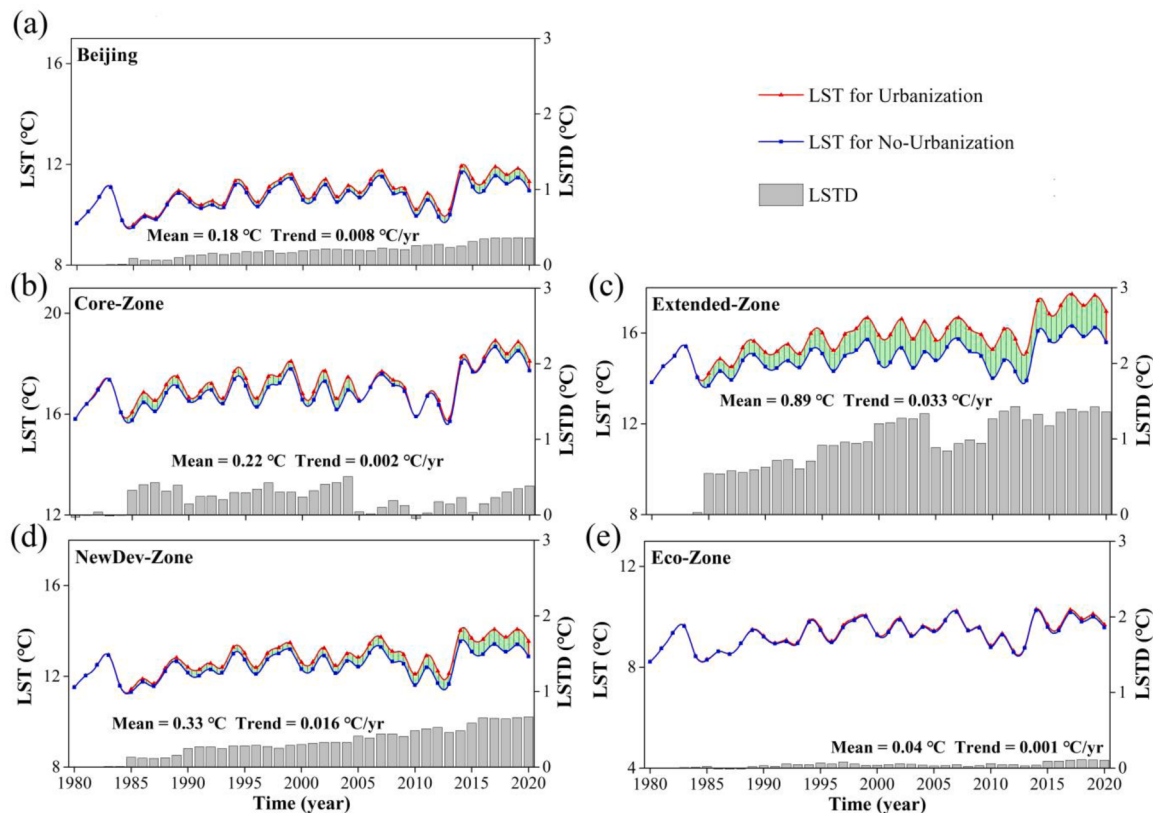


Fig. 6. The annual LST of the “urbanization” and the “no-urbanization” scenarios, and the LST difference (LSTD) between the two scenarios: (a) Beijing; (b) core-zone; (c) extended-zone; (d) NewDev-zone; and (e) eco-zone. The mean and trend values of LSTDs are presented in the figure.

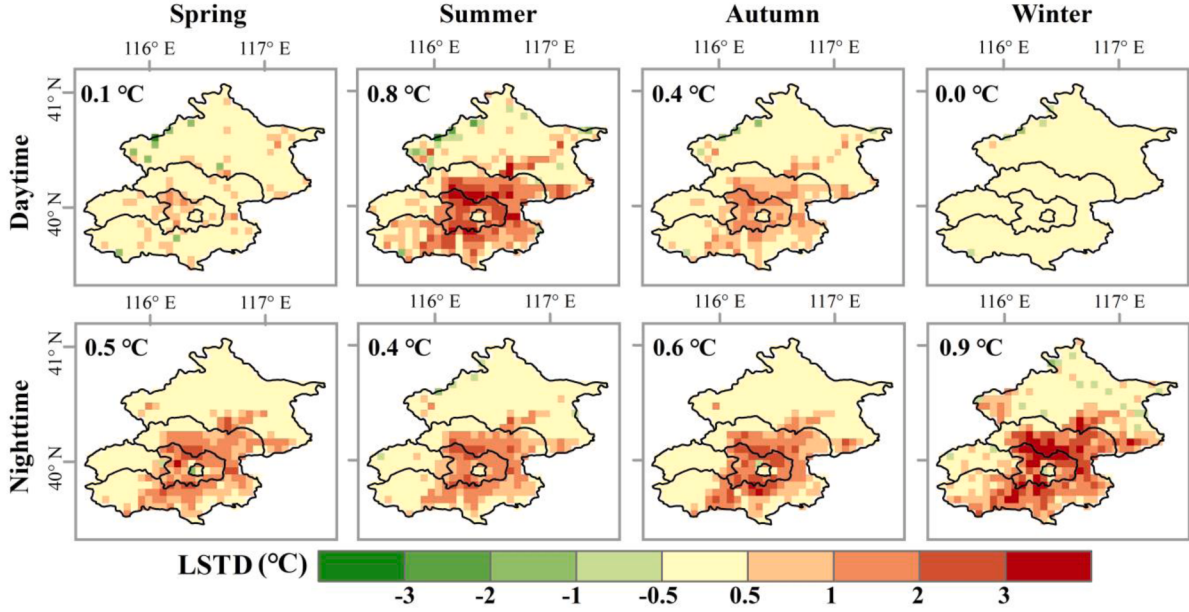


Fig. 7. The spatial distribution of the seasonal LSTD in daytime (6:00–18:00) and nighttime (18:00–6:00 in the next day) for 2015–2020.

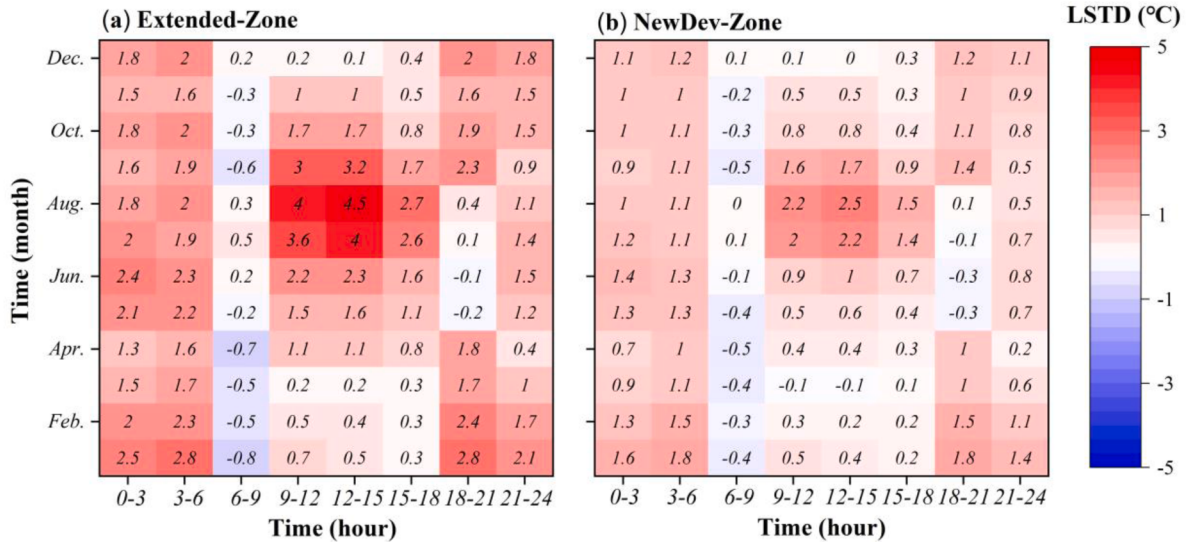


Fig. 8. The seasonal and diurnal cycles of LST Difference (LSTD) between the “urbanization” and “no-urbanization” scenarios during 2015–2020 periods: (a) extended-zone, and (b) NewDev-Zone.

1.9 °C for the Extended-Zone and 1.0 °C for the NewDev-Zone, followed by the autumn season (September to November), the values were approximately 1.4 °C for the Extended-Zone and 0.8 °C for the NewDev-Zone. The spring (March to May) LSTD showed the lowest value among the four seasons (~0.9 °C for Extended-Zone and 0.4 °C for NewDev-Zone).

For the diurnal comparison, the nighttime LSTD (18:00 to 6:00 in the next day) presented higher values comparing to the daytime LSTD (6:00 to 18:00), and the values were approximately 1.7 °C (Extended-Zone) and 1.0 °C (NewDev-Zone) during the nighttime, and 1.1 °C and 0.5 °C for the daytime period, respectively. Specifically, the greatest LSTDs generally took place in the 3:00–6:00, with the values of 2.0 °C in the Extended-Zone, and 1.2 °C in the NewDev-Zone. And the minimum LSTDs happened in 6:00–9:00, with the values lower than 0 °C in the two zones.

4.4. Overheating frequency and phenology

This study identified overheating consequences of urban growth according to the spatial distribution of frequency of heat days (FHD) in the two scenarios. As shown in Fig. 9, the average FHD in the Core-Zone was larger than 25% and presented slight changes during 1980–2020 in both the two scenarios. However, the FHD increased from approximately 16.3% (~60 days) in 1980–1984 to 24.1% (~88 days) in 2020 in the Extended-Zone, and from approximately 10.6–13.3% (39–49 days) in the NewDev-Zone along with urbanization. The high-FHD region thereby extended from the Core-Zone to the Extended-Zone and the NewDev-Zone in the “Urbanization” scenario. As for the “No-Urbanization” scenario, FHDs showed little change in the Extended-Zone and the NewDev-Zone, and the high-FHD region was mainly located in the Core-Zone.

To roughly quantify the impact of impervious surface on the heat

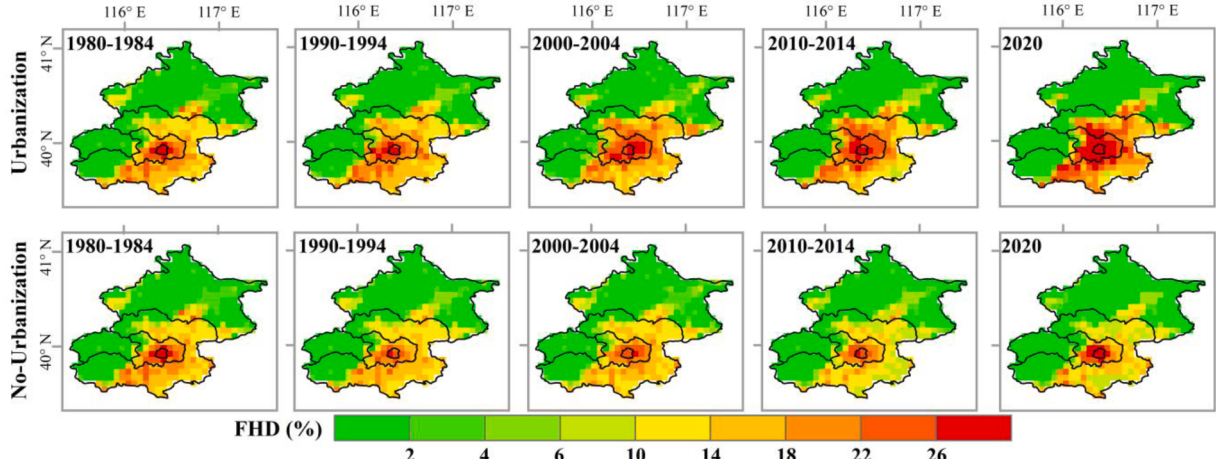


Fig. 9. The distribution of frequency of heat days (FHD) for the “urbanization” and “no-urbanization” scenarios in five time periods (1980–1984, 1990–1994, 2000–2004, 2010–2014, and 2020).

days, we plotted the average FHD against the associated average ISF for each grid cell in 2015–2020 (Fig. 10). It is interesting that, the annual FHD exhibited a strong linear correlation with the ISF after a relatively messy correlation. The threshold of ISF was about 25%. A rise in ISF of 1% may cause an increase in the annual FHD of 0.21% (0.77 days) when ISF beyond the threshold. The FHD therefore is up to 32% in places of 100% ISF according to the fitting formula, which means there may be about 120 heat days per year in a fully urbanized region (ISF = 100%) in Beijing.

The annual overheating duration and the timing of the peak-LST day were further detected for the Core-Zone, Extended-Zone and NewDev-Zone, as the three zones present high ISF or rapid urban growth (Fig. 11). The Core-Zone presented the longest overheating duration (~120 day of the year) from mid-May to mid-September, and showed slight changes in overheating durations for both the scenarios. The overheating durations of Extended-Zone and the NewDev-Zone were approximately 100 days and 60 days, and they extended at the rate of 5 and 4 day/decade in the “Urbanization” scenario, respectively. However, the overheating durations of the two zones were only approximately 80 and 40 days in the “No-Urbanization” scenario.

The thermal phenology changed in the past four decades. The timing of the peak-LST day generally located at mid-July, and it advanced in all the three zone in the “Urbanization” scenario. Specifically, the annual peak LST generally happened around 200th (July 19) in the Core-Zone, and 198th (July 17) and 195th (July 14) in the Extended-Zone and NewDev-Zone, respectively. The peak-LST day advanced from approximately 212th in 1980–1985 to 203th in 2015–2020 in the Core-Zone, with the rate of 3 day/decade. And the values for the Extended-Zone and NewDev-Zone were 209th to 203th and 211th to 202th, with

trends of approximately 2 and 3 day/decade, respectively. It is worth noting that the timing of the peak-LST day in the Extended-Zone showed stronger advancement in the “No-Urbanization” scenario than it in the “Urbanization” one. This situation can attribute to the higher peak LST in the “Urbanization” scenario: the average peak LST in Extended-Zone was about 37.2 °C in the “Urbanization” scenario, but only 35.4 °C in the “No-Urbanization” scenario.

5. Discussion

5.1. Estimation of LST

This study established seamless LST estimation during 1980–2020 for Beijing. The VIC model estimates temperature based on water and energy balance and associated heat transfer processes. The rainfall-runoff conversion process and thermal-related parameter modification within the model can effectively facilitate LST estimation in cities. Other than that, multiple satellite-based products (land cover maps, DSR, albedo, LAI, and FVC) were integrated into a physical model for LST simulation. The land cover maps and parameters were updated every five years to better depict the urban growth. The parameters of DSR, albedo, LAI, and FVC are highly related to energy balance, evapotranspiration and turbulent heat calculation, and are important for LST estimation (Paschalis et al., 2021; Zhang and Liang, 2018). Specifically, DSR is an essential component for total energy exchanges between the atmosphere and surface (Zhang et al., 2019). LAI, FVC, and albedo can reflect the land surface conditions and changes, such as urbanization, deforestation/afforestation (Liang et al., 2021). Thus, integrating the satellite-based products is capable of capturing the process of urbanization, as well as optimizing energy balance calculation and LST estimation in the physical framework. The simulated LST in our work presented satisfactory performance comparing with reference LST from the ground observations and the MODIS product.

Model-related method has advantages of customizing spatiotemporal resolution and coverage (Quan et al., 2014; Zhou et al., 2018), and can provide the LST information at a high spatio-temporal resolution and a long-term coverage relative to the ground-based observations and remote sensing datasets. For instance, the MODIS terra data only provide LST after 2000, with only two instantaneous records every day (Wan et al., 2002). Landsat and AVHRR can provide long-term observations (nearly four decades), but Landsat is only able to monitor LST records every 16 days (Arvidson et al., 2006), AVHRR shows low data quality as it is only available for cloudless sky (Deilami et al., 2018; Stathopoulou and Cartalis, 2009). Our work established a seamless LST data at 3-hour resolution for a long-term coverage (1980–2020), which facilitate the

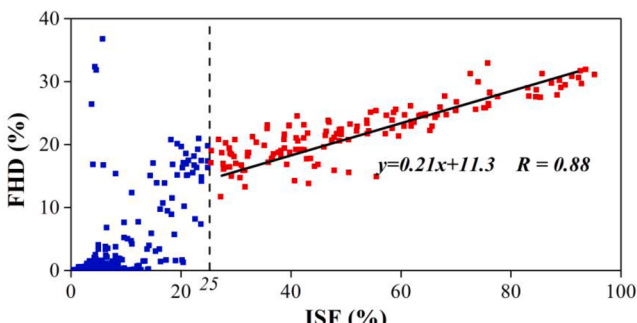


Fig. 10. The relationships of frequency of heat days (FHD) and ISF in 2015–2020.

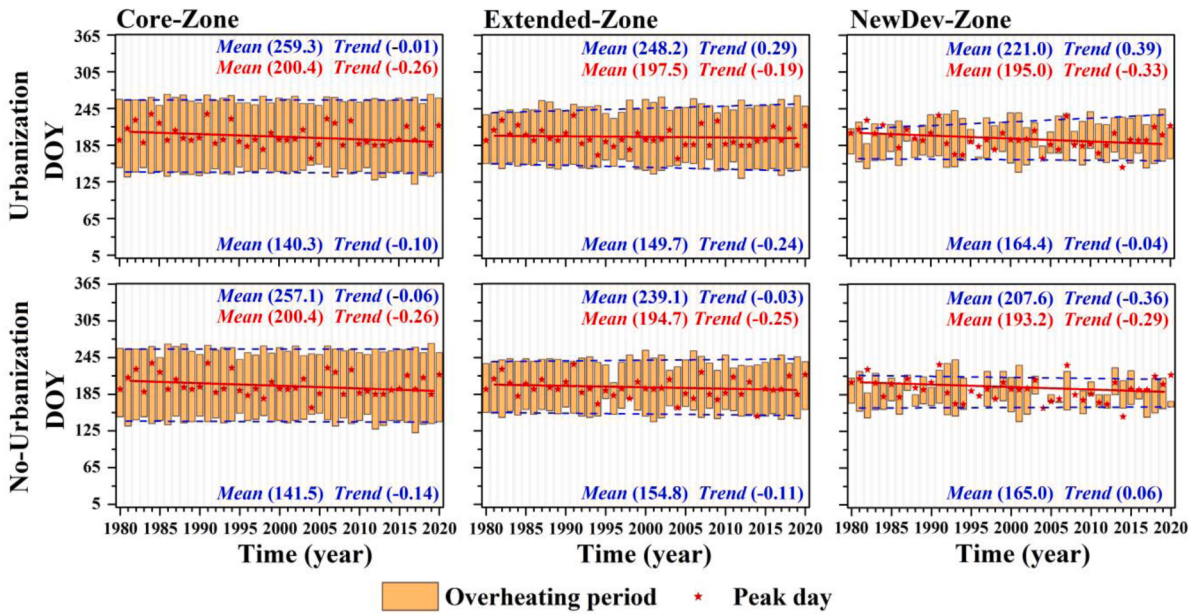


Fig. 11. The annual overheating durations and peak-LST day in core-zone, extended-zone and NewDev-zone during 1980–2020 in the two scenarios. The solid red line represents the trend of the peak-LST day, and the two blue dashed lines represent the trends of the onset and end of the overheating duration, respectively. The abbreviations DOY denote Day Of Year. The mean and trend values for the onset and end of the overheating durations and peak-LST day are shown in the figure.

quantification of LST and urban-induced LST changes at various temporal scales (diurnal, seasonal and annual). Also, the satisfactory LST validation in this study implies the capability of integrating satellite-based products with the urban monitoring. The method is therefore expected to have extensive application regarding water and energy fluxes.

5.2. LST variation and response to urban expansion

Based on the long-term LST estimates and experimental scenarios, our study quantified the impact of urbanization on LST in Beijing. The annual mean LST increased by 0.9 °C from 1980 to 1990 to 2010–2020 period in Beijing under “Urbanization” scenario, while the increase was only about 0.6 °C under “No-Urbanization” scenario. This phenomenon indicates that urbanization contributed to 33% of the land surface warming during 1980–2020. Ji et al. (2021) also quantified the effect of urbanization on LST in Beijing (1979–2017), and obtained a similar result (~31%) with our work. We conducted another comparative scenario with stable meteorological forcings (i.e., no changes in air temperature, precipitation, wind speed, humidity, and DSR) compares with “Urbanization” scenario, thereby isolating the impact of climate change on LST (Fig. 12). Climate change generally exerted relatively homogeneous effect on LST (~0.6 °C) in Beijing. The LST increase in the “No-Urbanization” scenario is thereby largely attributable to global climate change.

The urbanization effect on LST varied in Beijing, with more prominent effect in the urbanizing regions, i.e., the Extended-Zone (~1.3 °C) and the NewDev-Zone (~0.6 °C) for 2010–2020. Multiple researches also quantified the urban-induced LST changes in Beijing. Meng et al. (2018) characterized the spatio-temporal pattern of SUHI based on Landsat-8 and MODIS products, and found that the SUHI of approximately 1.86 °C (2003–2014). Wang et al. (2017) used the MODIS product, and showed that the SUHI ranged between 1.4–4.2 °C at four satellite overpass times during a day (2013–2014). The magnitude of the urbanization effect may vary with the study period, datasets, and urban/suburb boundary definitions (Kim and Brown, 2021; Meng et al., 2018). Our work adopted the model-related method to quantify the urban-induced LST changes (i.e., LSTD), thereby has the advantages of high temporal resolution of LST, and avoiding uncertainties in climate

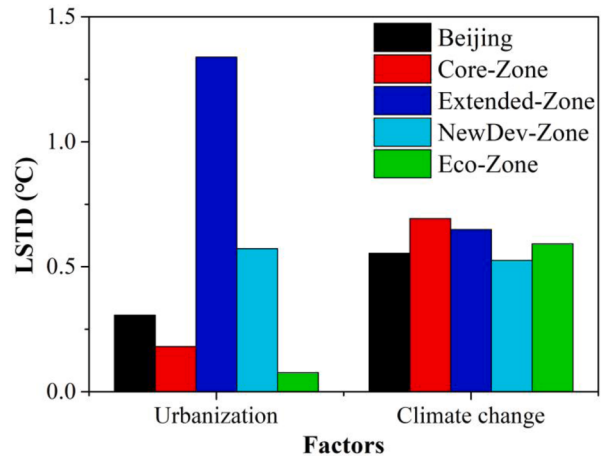


Fig. 12. The LSTD of the whole Beijing and the four zones during the 2010–2020 period. LSTD between “urbanization” and “no-urbanization” scenarios (left) denotes the urbanization effect, and LSTD between “urbanization” and “no-climate change” scenarios (right) denotes the climate change effect.

variability and boundary definitions.

Urbanization exerts different impact on daytime LST among seasons, with the largest impact in summer season. This phenomenon is mainly attributed to the reduction in thermal capacity and latent heat flux in cities (Cao et al., 2017). Specifically, summer season has large solar radiation and precipitation, resulting in higher energy input and more solar radiation-sensible heat conversion ratio in urban areas, thereby amplifying the urban-induced overheating (Peng et al., 2018; Taha, 1997). This effect is weaker in the other three seasons as for less solar radiation and precipitation. For the nighttime period, the urban-induced thermal effect showed less changes, but higher values comparing to that during daytime. The nighttime turbulent exchange generally lower than that in daytime period, resulting in a relatively stable and strong influence on nighttime LST. The nighttime LST highly related to the human activities and the heat storage from daytime (Zhou et al., 2018), thus the nighttime LSTD has the highest value in the winter season because of

more anthropogenic heating. Meng et al. (2018) and Wang et al. (2017) quantified the impact of urbanization on LST in Beijing based on the space-for-time approach, and also identified that the urban-induced daytime thermal effect has smaller values and stronger seasonal cycles. Our work used the model-related method, which is able to identify the spatio-temporal characteristics of urban-induced LST changes, as well as high-LST regions due to the urbanization.

Additionally, this study identified the changes of overheating frequency and phenology during the past four decades, and demonstrated increasing overheating duration and advancing peak-LST day corresponding to urban growth in Beijing. The annual FHD showed a linear correlation with the ISF in areas with an ISF beyond 25%, and the FHD may increase at a rate of 0.21% with every 1% rise of ISF. The threshold indicates that additional factors (e.g., forest cover and topography) may also influence FHD, causing a potentially weak impact of ISF on FHD when ISF is low. This threshold effect has also been reported in other studies, albeit with different response variables (Yang et al., 2011; Yeo and Guldmann, 2016). The urban expansion reshaped the heat phenology in Extended-Zone and NewDev-Zone: leading to earlier peak-LST day and longer overheating duration. The Core-Zone presented little change regarding the annual peak-LST day and the overheating durations, as this zone has been largely urbanized, and showed slight changes since 1980. The advance of peak-LST day has been mentioned in many meteorological reports, the phenomenon largely related to climatic factors such as warm air masses. The urban environment is more conducive to the energy cycle and sensitive to climate change, thereby promoting earlier peak-LST day. The transformation from natural ground to ISA will intensify LST, causing longer overheating duration (Bounoua et al., 2015; Peng et al., 2018; Wang et al., 2013).

5.3. Implication for the urban planning

The increase of LST in urban region threats people's health and living comfort, rises the electricity demand for cooling purposes (Santamouris, 2020). The thermal effect thereby raises considerable attention towards the heat mitigation strategies worldwide, including landscape configuration, blue-green space, rainwater wetlands, and cool roofs (He et al., 2019; Phelan et al., 2015; Yu et al., 2020). Decision-maker should consider increasing albedo and vegetation coverage through cool and green roofs in dense urban areas, and also, establish rational landscape configurations when developing new urban areas (e.g., close to water, incorporate with urban forestry, and confine local urban density).

The findings from this study may have implications for heat mitigation strategies. The Core-Zone and Extended-Zone are prone to overheating and FHD, as the two zones have the highest degree of urbanization. And the urbanization exhibited the highest thermal effects on summer daytime and winter nighttime, which may aggravate the overheating in summer season. Thus, heat mitigation strategies including cool and green roofs should focus on the Core-Zone and Extended-Zone, and summer season in Beijing. Moreover, our study suggests that 25% is a potential threshold, over which heat days can experience statistically significant changes due to ISF changes in Beijing. This threshold likely exists, because the land surface will become more homogeneous (i.e., dominated by impervious surface) and more influential to the LST as the ISF increase. The regional ISF therefore can be purposefully confined considering this threshold when developing new urban areas, or some heat remedies can be established in places with high ISF. Please note the value of 25% is just a rough estimate for the threshold, and it requires further studies concerning various urban areas and climate conditions.

Beijing is not alone with respect to urban expansion and related overheating threats. The land cover types and anthropogenic heat release, inevitably promote higher LST in urban areas. Urban-induced LST changes have been reflected in vast cities worldwide, including Italian metropolitan cities (Morabito et al., 2021), Phoenix (Li et al.,

2016b), Shanghai (Yue et al., 2012), and London (Kolokotroni et al., 2012). The impact of urbanization on LST may vary with climate backgrounds, but it is unquestionable that the LST will be intensified with the urban expansion, threatening our living comfort. Even worse, the urban-induced LST changes may overlap with global warming, further increasing potential overheating risk (Yan et al., 2016; Yao et al., 2021). Relevant policies including real-time urban monitoring, heat mitigation strategies, and emergency response programs should be strengthened to facilitate the management of urban environment, and remediation of potential overheating risks (He et al., 2019; Manoli et al., 2019).

5.4. Limitations

This study has limitations in the LST modeling, which may introduce uncertainties in the LST estimation and overheating analysis. One potential source of uncertainty is the model input data (e.g., vegetation and soil data). For example, we assumed that soil distribution remained relatively stable over time and used a constant soil map throughout the study period, while soil layers may change due to factors such as plant growth, climate change, and natural disasters. Second, while our study aims to identify the impact of urbanization on LST, the potential impact of other land cover activities also included, and may influence the urban environment (Yan and Zhou, 2023). However, the changes in non-urban land cover types in Beijing were relatively small over the past 40 years, and were captured at a lower spatial resolution of 1 km.

Third, our work adjusted three thermal-related parameters (i.e., albedo, k , and C_s) in VIC model based on the MODIS LST product that includes the influence of human activities and buildings. However, buildings, anthropogenic heat and landscape structure are complex and highly interactive in cities (Li et al., 2019) which are important in urban models (Ji et al., 2021; Meili et al., 2020). Considering only three parameters of thermal properties may bring uncertainties for LST estimation in urban environment. Moreover, the LST simulation was conducted at 3-hour time step, while the MODIS product can only provide two instantaneous LST records. Uncertainty may exist in LST estimation and evaluation as for different spatio-temporal resolution, especially for periods without observed data (e.g., 6:00–9:00, 12:00–15:00). The model methods with 3-hour temporal resolution may potentially smooth peaks and troughs in the frequency of heat days and the duration of extreme heat events, thereby possibly disregarding certain heat waves. Therefore, finer resolution of the LST modeling, more evaluation products, and specific urban module or more thermal parameters of ISA should be developed and considered in the future work.

6. Conclusions

This study characterized the spatial and temporal dynamics of LST for the period of 1980–2020 at 3 h resolution in Beijing, and identified the response of LST to the urban growth based on the modified VIC model and multiple satellite products. The approach demonstrated reliable performance as the simulated LST showed high consistency with MODIS retrievals and ground-based observations. Other than the space-for-time approach (i.e., SUHI) used by many other researches, our work established comparative scenarios with dynamic and constant land cover information, respectively, thereby directly evidencing the urban-induced LST changes. Our study achieved a few interesting conclusions:

- (1) The mean annual LST increased from approximately 10.3 °C in 1980–1990 to 11.2 °C in 2010–2020 for Beijing as a whole, with only one third attributable to the ISA expansion. However, the regions with rapid urbanization (i.e., Extended-Zone and NewDev-Zone) generally show the highest LST increase (~1.9 and 1.2 °C), with over a half contributed by the ISA expansion.
- (2) The four-decade and 3-hourly LST estimates revealed that the thermal effect of urbanization has seasonal and diurnal

- distinction. The thermal effect is generally stronger in nighttime than it in daytime, except for the summer season. The urban-induced thermal effect is quite strong during summer daytime and winter nighttime.
- (3) Urbanization likely enhanced the frequency of heat days and reshaped the heat phenology. The frequency was likely to increase about 0.21% (0.77 days) along with each 1% increase in the ISF for regions with ISF above a threshold. The Extended-Zone and the NewDev-Zone experienced rapid urbanization, thereby facing obvious enhanced FHD, prolonged overheating duration (4~5 days/decade), and advanced peak-LST day (2~3 days/decade).

This study has limitations due to the fact that the modeling has a relatively-coarse spatial resolution (~5 km) and it failed to reflect the thermal and hydrological interactions over different urban surfaces. Despite the uncertainties in the LST estimation, this study has advantages of characterizing spatio-temporal dynamic of LST at a short time step (3-hour), and quantifying the thermal effect of urbanization at various temporal scales (diurnal, seasonal, and annual) in Beijing. Moreover, our work identified the obvious urban-induced increases of LST during summer daytime period, and the prolonged overheating durations in urbanizing areas. The findings could provide implications for urban planning and heat mitigation construction for Beijing and other similar megacities. To obtain more accurate and detailed LST information and the urban-related LST changes, future studies could develop finer-resolution model frameworks and consider more reasonable physical processes with associated thermal parameters of ISA according to the building structures.

Declaration of Competing Interest

The authors declare that they have no known competing financial interests or personal relationships that could have appeared to influence the work reported in this paper.

Data Availability

Data will be made available on request.

Acknowledgement

This study was supported by grants from the National Natural Science Foundation of China (No. 41971030) and the Open Fund of State Key Laboratory of Remote Sensing Science and Beijing Engineering Research Center for Global Land Remote Sensing Products (No. OF202204). Acknowledgement for the data support from “National Earth System Science Data Center, National Science & Technology Infrastructure of China (<http://www.geodata.cn>) and MODerate-resolution Imaging Spectroradiometer (<https://modis.gsfc.nasa.gov/>). The GLASS products can be downloaded at www.glass.umd.edu.

References

- Arvidson, T., Goward, S., Gasch, J., Williams, D., 2006. Landsat-7 long-term acquisition plan: development and validation. *Photogramm. Eng. Remote Sensing* 72 (10), 1137–1146.
- Bounoua, L., et al., 2015. Impact of urbanization on US surface climate. *Environ. Res. Lett.* 10 (8), 084010.
- Cao, C., li, X., Zhang, M., Liu, S., Xu, J., 2017. Correlation Analysis of the Urban Heat Island Effect and Its Impact Factors in China. *Environ. Sci.* 38 (10), 3987–3997.
- Cui, Y., Yan, D., Hong, T., Ma, J., 2017. Temporal and spatial characteristics of the urban heat island in Beijing and the impact on building design and energy performance. *Energy* 130, 286–297.
- Dai, Y., et al., 2013. Development of a China dataset of soil hydraulic parameters using pedotransfer functions for land surface modeling. *J. Hydrometeorol.* 14 (3), 869–887.
- Danielson, J.J. and Gesch, D.B., 2011. Global multi-resolution terrain elevation data 2010 (GMTED2010). U.S. Geological Survey Open-File Report, 2011-1073: 26.
- Deilami, K., Kamruzzaman, M., Liu, Y., 2018. Urban heat island effect: a systematic review of spatio-temporal factors, data, methods, and mitigation measures. *Int. J. Appl. Earth Obs. Geoinf.* 67, 30–42.
- Ding, T., Qian, W., Yan, Z., 2010. Changes in hot days and heat waves in China during 1961–2007. *Int. J. Climatol.* 30 (10), 1452–1462.
- Giannaros, C., Nenes, A., Giannaros, T.M., Kourtidis, K., Melas, D., 2018. A comprehensive approach for the simulation of the Urban Heat Island effect with the WRF/SLUCM modeling system: the case of Athens (Greece). *Atmos. Res.* 201, 86–101.
- Gong, P., Li, X., Zhang, W., 2019. 40-Year (1978–2017) human settlement changes in China reflected by impervious surfaces from satellite remote sensing. *Sci. Bull.* 64 (11), 756–763.
- Guli, J., Liang, S., Yi, Q., Liu, J., 2015. Vegetation dynamics and responses to recent climate change in Xinjiang using leaf area index as an indicator. *Ecol. Indic.* 58, 64–76.
- Hao, L., et al., 2018. Ecohydrological processes explain urban dry island effects in a wet region, Southern China. *Water Resour. Res.* 54 (9), 6757–6771.
- He, B.-J., et al., 2019. Co-benefits approach: opportunities for implementing sponge city and urban heat island mitigation. *Land Use Policy* 86, 147–157.
- Hu, Y., et al., 2015. The cumulative effects of urban expansion on landsurface temperatures in metropolitan Jingjintang, China. *J. Geophys. Res.: Atmos.* 120, 9932–9943.
- Jang, J., Lee, W., Choi, M., Kang, C., Kim, H., 2020. Roles of urban heat anomaly and land-use/land-cover on the heat-related mortality in the national capital region of South Korea: a multi-districts time-series study. *Environ. Int.* 145, 106127.
- Ji, P., et al., 2021. High-resolution land surface modeling of the effect of long-term urbanization on hydrothermal changes over Beijing metropolitan area. *J. Geophys. Res.: Atmos.* 126 (18), e2021JD034787.
- Jia, K., et al., 2019. Long-term global land surface satellite (GLASS) fractional vegetation cover product derived from MODIS and AVHRR data. *IEEE J. Sel. Top. Appl. Earth Obs. Remote Sens.* 12 (2), 508–518.
- Jiang, F., et al., 2022. Vegetation greening intensified transpiration but constrained soil evaporation on the Loess Plateau. *J. Hydrol.* 614, 128514.
- Kim, S.W., Brown, R.D., 2021. Urban heat island (UHI) intensity and magnitude estimations: a systematic literature review. *Sci. Total Environ.* 779, 146389.
- Kolokotroni, M., Ren, X., Davies, M., Mavrogianni, A., 2012. London's urban heat island: impact on current and future energy consumption in office buildings. *Energy Build.* 47, 302–311.
- Li, D., et al., 2019. Urban heat island: aerodynamics or imperviousness? *Sci. Adv.* 5 (4), eaau4299.
- Li, Z.-L., et al., 2023. Satellite remote sensing of global land surface temperature: Definition, methods, products, and applications. *Rev. Geophys.* 61 (1) e2022RG000777.
- Li, D., Malyshev, S., Sheviakova, E., 2016a. Exploring historical and future urban climate in the earth system modeling framework: 2. Impact of urban land use over the Continental United States. *J. Adv. Model. Earth Syst.* 8 (2), 936–953.
- Li, K., Chen, Y., Gao, S., 2022. Uncertainty of city-based urban heat island intensity across 1112 global cities: background reference and cloud coverage. *Remote Sens. Environ.* 271, 112898.
- Li, X., et al., 2016b. Remote sensing of the surface urban heat island and land architecture in Phoenix, Arizona: combined effects of land composition and configuration and cadastral-demographic-economic factors. *Remote Sens. Environ.* 174, 233–243.
- Liang, S., et al., 2021. The global land surface satellite (GLASS) products suite. *Bull. Am. Meteorol. Soc.* 102, E323–E337.
- Liang, X., Lettenmaier, D.P., Wood, E.F., Burges, S.J., 1994. A simple hydrologically based model of land surface water and energy fluxes for general circulation models. *J. Geograph. Res.* 99 (D7), 14415–14428.
- Liang, X., Wood, E.F., Lettenmaier, D.P., 1996. Surface soil moisture parameterization of the VIC-2L model: evaluation and modification. *Glob. Planet Change* 13, 195–206.
- Liang, X., Xie, Z., 2001. A new surface runoff parameterization with subgrid-scale soil heterogeneity for land surface models. *Adv. Water Resour.* 24, 1173–1193.
- Liu, J., et al., 2010. Spatial patterns and driving forces of land use change in China during the early 21st century. *J. Geog. Sci.* 20 (4), 483–494.
- Liu, Q., et al., 2013. Preliminary evaluation of the long-term GLASS albedo product. *Int. J. Digital Earth* 6 (sup1), 69–95.
- Liu, Q., Zhang, S., Zhang, H., Bai, Y., Zhang, J., 2020a. Monitoring drought using composite drought indices based on remote sensing. *Sci. Total Environ.* 711, 134585.
- Liu, X., et al., 2020b. Spatiotemporal patterns of summer urban heat island in Beijing, China using an improved land surface temperature. *J. Clean. Prod.* 257, 120529.
- Manoli, G., et al., 2019. Magnitude of urban heat islands largely explained by climate and population. *Nature* 573 (7772), 55–60.
- Masson, V., et al., 2020. City-descriptive input data for urban climate models: Model requirements, data sources and challenges. *Urban Climate* 31, 100536.
- Meili, N., et al., 2020. An urban ecohydrological model to quantify the effect of vegetation on urban climate and hydrology (UT&C v1.0). *Geosci. Model. Dev.* 13 (1), 335–362.
- Meili, N., et al., 2021. Tree effects on urban microclimate: diurnal, seasonal, and climatic temperature differences explained by separating radiation, evapotranspiration, and roughness effects. *Urban Forest. Urban Greening* 58, 126970.
- Meng, Q., et al., 2018. Characterizing spatial and temporal trends of surface urban heat island effect in an urban main built-up area: a 12-year case study in Beijing, China. *Remote Sens. Environ.* 204, 826–837.

- Meng, S., Xie, X., Zhu, B., Wang, Y., 2020. The relative contribution of vegetation greening to the hydrological cycle in the Three-North region of China: a modelling analysis. *J. Hydrol.* 591, 125689.
- Meyer, D., et al., 2020. WRF-TEB: implementation and evaluation of the coupled weather research and forecasting (WRF) and town energy balance (TEB) model. *J. Adv. Model. Earth Syst.* 12 (8), e2019MS001961.
- Miles, V., Esau, I., 2020. Surface urban heat islands in 57 cities across different climates in northern Fennoscandia. *Urban Climate* 31, 100575.
- Mishra, V., et al., 2010. A regional scale assessment of land use/land cover and climatic changes on water and energy cycle in the upper Midwest United States. *Int. J. Climatol.* 30 (13), 2025–2044.
- Morabito, M., et al., 2021. Surface urban heat islands in Italian metropolitan cities: tree cover and impervious surface influences. *Sci. Total Environ.* 751, 142334.
- Nijssen, B., Schnur, R., Lettenmaier, P., 2001. Global retrospective estimation of soil moisture using the variable infiltration capacity land surface model, 1980–93. *J. Clim.* 14, 1790–1808.
- Niu, L., Tang, R., Jiang, Y., Zhou, X., 2020. Spatiotemporal patterns and drivers of the surface urban heat island in 36 major Cities in China: a comparison of two different methods for delineating rural areas. *Sustainability* 12 (2), 478.
- Oke, T.R., Stewart, I.D., 2012. Local climate zones for urban temperature studies. *Bull. Am. Meteorol. Soc.* 93 (12), 1879–1900.
- Oleson, K.W., Feddema, J., 2020. Parameterization and surface data improvements and new capabilities for the community land model urban (CLMU). *J. Adv. Model. Earth Syst.* 12 (2) e2018MS001586.
- Paschalis, A., Chakraborty, T.C., Fatichi, S., Meili, N., Manoli, G., 2021. Urban forests as main regulator of the evaporative cooling effect in cities. *AGU Adv.* 2 (2) e2020AV000303.
- Peng, J., Jia, J., Liu, Y., Li, H., Wu, J., 2018. Seasonal contrast of the dominant factors for spatial distribution of land surface temperature in urban areas. *Remote Sens. Environ.* 215, 255–267.
- Peng, J., Xie, P., Liu, Y., Ma, J., 2016. Urban thermal environment dynamics and associated landscape pattern factors: a case study in the Beijing metropolitan region. *Remote Sens. Environ.* 173, 145–155.
- Phelan, P.E., et al., 2015. Urban heat island: mechanisms, implications, and possible remedies. *Annu. Rev. Environ. Resour.* 40 (1), 285–307.
- Piao, S., et al., 2015. Detection and attribution of vegetation greening trend in China over the last 30 years. *Glob Chang. Biol.* 21 (4), 1601–1609.
- Pumo, D., Arnone, E., Francipane, A., Caraciolo, D., Noto, L.V., 2017. Potential implications of climate change and urbanization on watershed hydrology. *J. Hydrol.* 554, 80–99.
- Qiao, Z., Tian, G., Zhang, L., Xu, X., 2014. Influences of urban expansion on urban heat island in Beijing during 1989–2010. *Adv. Meteorol.* 2014, 1–11.
- Quan, J., et al., 2014. Multi-temporal trajectory of the urban heat island centroid in Beijing, China based on a Gaussian volume model. *Remote Sens. Environ.* 149, 33–46.
- Rao, P.K., 1972. Remote Sensing of Urban Heat Islands from an Environmental Satellite. *Bull. Am. Meteorol. Soc.* 53, 647–648.
- Santamouris, M., 2020. Recent progress on urban overheating and heat island research. Integrated assessment of the energy, environmental, vulnerability and health impact. Synergies with the global climate change. *Energy Build.* 207, 109482.
- Stathopoulou, M., Cartalis, C., 2009. Downscaling AVHRR land surface temperatures for improved surface urban heat island intensity estimation. *Remote Sens. Environ.* 113 (12), 2592–2605.
- Sun, T., Grimmond, S., 2019. A Python-enhanced urban land surface model SuPy (SUEWS in Python, v2019.2): development, deployment and demonstration. *Geosci. Model. Dev.* 12 (7), 2781–2795.
- Taha, H., 1997. Urban climates and heat islands albedo, evapotranspiration, and anthropogenic heat. *Energy Build.* 25, 99–104.
- Taha, Haider, 1999. Modifying a mesoscale meteorological model to better incorporate urban heat storage. *A. J. Appl. Meteorol.* 38 (4), 466–473.
- UN, 2018. United Nations Population Division World Urbanization Prospects: The 2018 Revision. Online Edition. <https://population.un.org/wup/>.
- Wan, Z., Zhang, Y., Zhang, Q., Li, Z.-l., 2002. Validation of the land-surface temperature products retrieved from Terra moderate resolution imaging spectroradiometer data. *Remote Sens. Environ.* 83 (1), 163–180.
- Wang, D., Liang, S., He, T., Shi, Q., 2015. Estimation of daily surface shortwave net radiation from the combined MODIS data. *IEEE Trans. Geosci. Remote Sens.* 53 (10), 5519–5529.
- Wang, J., Yan, Z., Li, Z., Liu, W., Wang, Y., 2013. Impact of urbanization on changes in temperature extremes in Beijing during 1978–2008. *Chin. Sci. Bull.* 58 (36), 4679–4686.
- Wang, K., et al., 2017. Comparing the diurnal and seasonal variabilities of atmospheric and surface urban heat islands based on the Beijing urban meteorological network. *J. Geophys. Res.: Atmos.* 122, 2131–2154.
- Wang, Y., et al., 2020. Quantifying the response of potential flooding risk to urban growth in Beijing. *Sci. Total Environ.* 705, 135868.
- Wang, Y., et al., 2022. Accelerated hydrological cycle on the Tibetan Plateau evidenced by ensemble modeling of Long-term water budgets. *J. Hydrol.* 615, 128710.
- Wei, S., et al., 2013. A China data set of soil properties for land surface modeling. *J. Adv. Model. Earth Syst.* 5 (2), 212–224.
- Wu, D., Xie, X., Tong, J., Meng, S., Wang, Y., 2020. Sensitivity of vegetation growth to precipitation in a typical afforestation area in the loess plateau: plant-water coupled modelling. *Ecol. Modell.* 430, 109128.
- Xiao, Z., et al., 2016. Long-time-series global land surface satellite leaf area index product derived from MODIS and AVHRR surface reflectance. *IEEE Trans. Geosci. Remote Sens.* 54 (9), 5301–5318.
- Xie, X., et al., 2015. Detection and attribution of changes in hydrological cycle over the three-north region of China: climate change versus afforestation effect. *Agric. For. Meteorol.* 203, 74–87.
- Yan, Z.-W., Wang, J., Xia, J.-J., Feng, J.-M., 2016. Review of recent studies of the climatic effects of urbanization in China. *Adv. Climate Change Res.* 7 (3), 154–168.
- Yan, Z., Zhou, D., 2023. Rural agriculture largely reduces the urban heating effects in China: a tale of the three most developed urban agglomerations. *Agric. For. Meteorol.* 331, 109343.
- Yang, G., Bowling, L.C., Cherkauer, K.A., Pijanowski, B.C., 2011. The impact of urban development on hydrologic regime from catchment to basin scales. *Landsc. Urban Plan.* 103 (2), 237–247.
- Yang, G., Bowling, L.C., Cherkauer, K.A., Pijanowski, B.C., Niyogi, D., 2010. Hydroclimatic response of watersheds to urban intensity: an observational and modeling-based analysis for the White River Basin, Indiana. *J. Hydrometeorol.* 11 (1), 122–138.
- Yang, P., Ren, G., Liu, W., 2013. Spatial and Temporal Characteristics of Beijing Urban Heat Island Intensity. *J. Appl. Meteorol. Climatol.* 52 (8), 1803–1816.
- Yang, W.R., Li, F., He, Y., 2014. Characteristic change and analysis of urban heat island in Beijing, China, Summer, 2003–2011. *Acta Ecologica Sinica* 34 (15), 4390–4399.
- Yao, R., et al., 2021. Long-term trends of surface and canopy layer urban heat island intensity in 272 cities in the mainland of China. *Sci. Total Environ.* 772, 145607.
- Yeo, I.-Y., Guldmann, J.-M., 2016. Land-use optimization for controlling peak flow discharge and nonpoint source water pollution. *Environ. Plann. B* 33 (6), 903–921.
- Yu, Z., et al., 2020. Critical review on the cooling effect of urban blue-green space: a threshold-size perspective. *Urban Forest. Urban Green.* 49, 126630.
- Yuan, G., et al., 2022. Impacts of afforestation on land surface temperature in different regions of China. *Agric. For. Meteorol.* 318, 108901.
- Yue, W., Liu, Y., Fan, P., Ye, X., Wu, C., 2012. Assessing spatial pattern of urban thermal environment in Shanghai, China. *Stochastic Environ. Res. Risk Assess.* 26 (7), 899–911.
- Zhang, X., et al., 2016. Local adaptive calibration of the satellite-derived surface incident shortwave radiation product using smoothing spline. *IEEE Trans. Geosci. Remote Sens.* 54 (2), 1156–1169.
- Zhang, X., et al., 2019. An operational approach for generating the global land surface downward shortwave radiation product from MODIS data. *IEEE Trans. Geosci. Remote Sens.* 57 (7), 4636–4650.
- Zhang, Y., Liang, S., 2018. Impacts of land cover transitions on surface temperature in China based on satellite observations. *Environ. Res. Lett.* 13 (2), 024010.
- Zhao, L., Lee, X., Smith, R.B., Oleson, K., 2014. Strong contributions of local background climate to urban heat islands. *Nature* 511 (7508), 216–219.
- Zhao, X., et al., 2013. The global land surface satellite (GLASS) remote sensing data processing system and products. *Remote Sens.* 5 (5), 2436–2450.
- Zhou, D., et al., 2018. Satellite remote sensing of surface urban heat islands: progress, challenges, and perspectives. *Remote Sens.* 11 (1), 48.
- Zhou, D., Xiao, J., Frolking, S., Zhang, L., Zhou, G., 2022. Urbanization contributes little to global warming but substantially intensifies local and regional land surface warming. *Earth's Future* 10 (5), e2021EF002401.
- Zhou, J., Li, J. and Yue, J., 2010. Analysis of urban heat island (UHI) in the Beijing. IGARSS: 3327–3330.
- Zhu, B., et al., 2021. Extensive evaluation of a continental-scale high-resolution hydrological model using remote sensing and ground-based observations. *Remote Sens.* 13 (7), 1247.
- Zhu, B., Xie, X., Meng, S., Lu, C., Yao, Y., 2020. Sensitivity of soil moisture to precipitation and temperature over China: present state and future projection. *Sci. Total Environ.* 705, 135774.
- Zhu, B., Xie, X., Wang, Y., Zhao, X., 2023. The benefits of continental-scale high-resolution hydrological modeling in the detection of extreme hydrological events in China. *Remote Sens.* 15 (9), 2402.
- Zhu, Z., et al., 2016. Greening of the Earth and its drivers. *Nat. Clim. Chang.* 6 (8), 791–795.